Fermiology of ZrTe with triply degenerate nodes and highly anisotropic magnetization

W. L. Zhu,[1,3,*] J. B. He,[1,2,*] Y. J. Xu,[1,3] S. Zhang,[1] D. Chen,[1] L. Shan,[1,3] Y. F. Yang,[1,3,4] Z. A. Ren,[1,3,4] G. Li,[1,3,4,†] and G. F. Chen[1,3,4,‡]

[1]*Institute of Physics and Beijing National Laboratory for Condensed Matter Physics, Chinese Academy of Sciences, Beijing 100190, China*
[2]*College of Physics and Electronic Engineering, Nanyang Normal University, Nanyang 473061, China*
[3]*School of Physical Sciences, University of Chinese Academy of Sciences, Beijing 100190, China*
[4]*Songshan Lake Materials Laboratory, Dongguan, Guangdong 523808, China*

(Received 18 December 2018; accepted 14 May 2020; published 8 June 2020)

ZrTe was recently predicted to be a new type of three-dimensional topological semimetal (TSM) hosting triply degenerate point nodes close to Fermi energy. Here experimental results of magnetotransport and magnetization on single crystals of ZrTe are reported. The bulk electronic structure of the material is studied by quantum oscillations in both resistivity and magnetization, combined with first-principles calculations. ZrTe is a multiband system with both electron and hole charge carriers. Several small three-dimensional Fermi surfaces with light effective masses are observed. The magnetization at low temperature with field along the C_3 symmetry axis is paramagnetic and has a $H^{0.5}$ dependence at high field, in contrast to the diamagnetic response observed for in-plane magnetization. The compound provides a platform to explore exotic quantum phenomena related to the three-component fermionic quasiparticles distinct from other known TSMs.

DOI: 10.1103/PhysRevB.101.245127

I. INTRODUCTION

There are rapid developments in the research on topological semimetals (TSMs) in condensed-matter physics and material science since characterizing a material by the topology of its electronic band structure has been more widely recognized for metallic systems and with discoveries of exotic physical phenomena as well as possible future device applications [1–3]. Because of the difference in symmetry required to stabilize the band crossing points (nodes) near the Fermi level, the TSMs are categorized into several subfamilies according to the degeneracy of the spin state and momentum space distribution of the nodes. There are Dirac semimetals [4–9] with fourfold-degenerate nodes, Weyl semimetals [10–13] with paired, twofold-degenerate Weyl nodes, and nodal-line semimetals, with bands crossing in the form of a periodically continuous line or closed ring in momentum space [14,15].

Recent theoretical studies have further suggested that in crystalline systems, band crossing points with three-, six-, or eightfold degeneracies is possible [16]. Triply degenerate points (TPs) can either be stabilized in space groups with nonsymmorphic symmetry at high-symmetry points or inversion-asymmetric crystals with a threefold rotation axis and a mirror plane along high-symmetry lines [16–20]. For the latter, material prediction includes MoP, WC, ZrTe, and TaN. Subsequently, angle-resolved photoemission spectroscopy (ARPES) indicated the presence of TPs in MoP [21]. However, since those TPs lie about 1 eV below E_F, their influence on the transport properties is unclear [22]. A recent ARPES [23] measurement showed that TPs of WC are closer to E_F, while its transport properties are similar to other TSMs [24]. Searching for properties that are unique to the "new fermions" is of high interest, while experimentally, a crucial step is to determine the bulk electronic structure.

In this work, we successfully grow single crystals of WC-type ZrTe. Compared to other materials proposed in the same class, in ZrTe by calculation the TPs are within 100 meV of E_F [17], and the band dispersions are relatively simple, thus making it a good candidate for further studies and possible tuning. Magnetotransport and magnetization measurements are performed and compared with other known TSMs. The hole-type carriers with high mobility dominate electric transport at low temperature. By studying Shubnikov–de Haas (SdH) and de Haas–van Alphen (dHvA) quantum oscillations (QO) combined with calculation, the bulk electronic structure is determined. It is three-dimensional (3D) and has both tiny electron and hole Fermi surfaces (FSs), including one hole FS in a toroid shape. The anisotropy and field dependence of magnetization at low temperature and high field are observed, whether it is connected to the Landau level spectra close to the triply degenerate node requires further investigation.

II. EXPERIMENTAL AND CALCULATION DETAILS

The single crystals of WC-type ZrTe were grown from indium flux. Zr, Te, and In with a molar ratio of 1:1:60 were put into an alumina crucible and sealed in an evacuated quartz tube. The quartz tube was heated to 1000 °C and then cooled at a speed of 1 °C/h to 500 °C, at which point the In was decanted by centrifugation. The obtained single crystals are hexagonal shaped with sides of ∼0.5 mm and thickness of ∼0.4 mm. The single crystals were characterized by x-ray diffraction (XRD) on a PANalytical diffractometer with Cu

*These authors contributed equally to this work.
†gli@iphy.ac.cn
‡gfchen@iphy.ac.cn

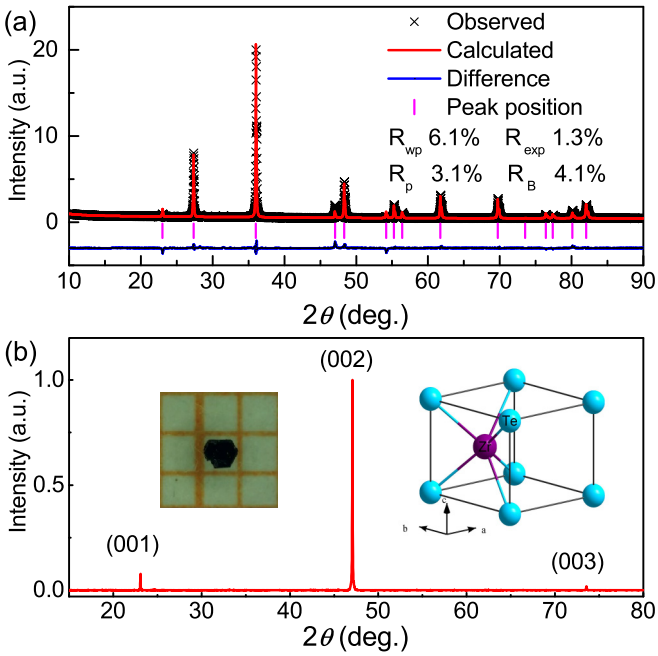

FIG. 1. Crystal structure of ZrTe. (a) Powder XRD spectrum of WC-type ZrTe at room temperature and refinement. (b) The single-crystal XRD of (00l) reflections, indicating that the crystal grows well along the *ab* plane. An optical image of a grown single crystal on a millimeter grid and the crystal structure are shown in the insets.

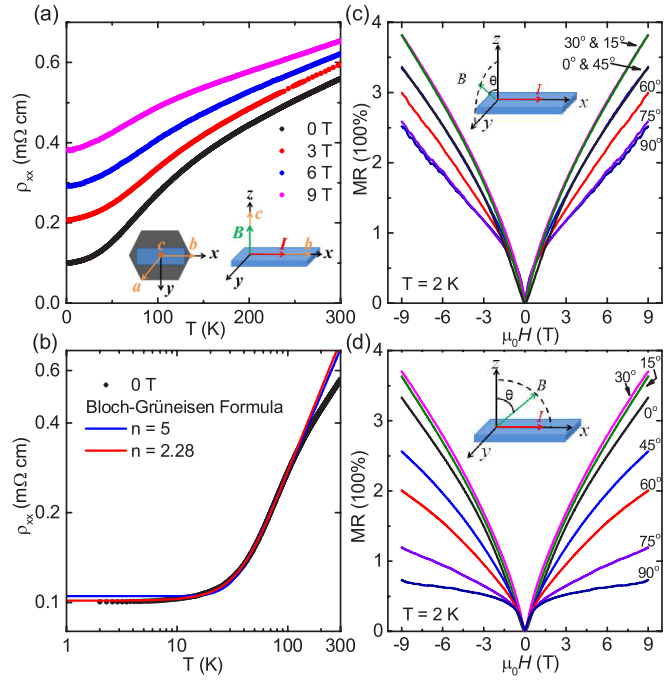

FIG. 2. Electrical transport properties of WC-type ZrTe. The sample geometry with respect to the crystalline axis and measurement configurations are illustrated. The z direction is the C_3 axis. (a) Temperature dependence of ρ_{xx} under magnetic fields with $H \parallel z$. (b) Bloch-Grüneisen fit of zero field $\rho(T)$ (see text). (c) and (d) Magnetic field dependence of resistivity at 2 K with H rotated in the yz and xz planes, respectively.

$K\alpha$ radiation at room temperature. The element compositions were determined by Oxford X-Max energy dispersive x-ray (EDX) spectroscopy analysis on a Hitachi S-4800 scanning electron microscope. Temperature- and field-dependent resistivity measurements on oriented single crystals were performed using a Quantum Design physical property measurement system. DC magnetization was measured by a vibrating-sample magnetometer superconducting quantum interference device. Torque magnetization experiments using cantilevers were performed at the National High Magnetic Field Laboratory, Tallahassee, in both superconducting and resistive magnets. The change in torque was read out by the change in capacitance by a digital bridge.

First-principles calculations were performed with the WIEN2K package [25] using the full-potential linearized augmented plane-wave method. The generalized gradient approximation (GGA) of Perdew-Burke-Ernzerhof type (GGA-PBE) [26] was employed. The plane-wave cutoff was set to $R_{MT}K_{\mathrm{MAX}} = 7$, and 150 000 k points in the first Brillouin zone (BZ) were used. Experimental lattice parameters were taken as input.

III. RESULTS AND DISCUSSION

As shown in Fig. 1, all the peaks can be indexed in a hexagonal WC-type crystal structure with space group $P\bar{6}m2$ (No. 187) by the Rietveld refinement program, TOPAS ACADEMIC [27]. The refined lattice parameters, $a = b = 3.764(1)$ Å and $c = 3.860(1)$ Å, are in good agreement with the reported values [28]. The average Zr:Te atomic ratio determined by EDX is very close to unity, and no foreign element was detected within the instrument resolution.

Figure 2(a) shows the temperature dependence of resistivity $\rho_{xx}(T)$ by the standard four-probe method under various magnetic fields with $H \| z$ and $I \| x$. At zero field, $\rho_{xx}(T)$ shows a metallic behavior with a moderately large residual resistivity of ~0.1 mΩ cm, and the residual resistivity ratio [RRR = $\rho_{xx}(300\ \mathrm{K})/\rho_{xx}(2\ \mathrm{K})$] is about 5. A simulation of $\rho(T)$ is tested by the Bloch-Grüneisen formula [29]:

$$\rho(T) = \rho_0 + C\left(\frac{T}{\Theta_R}\right)^n \int_0^{\Theta_R/T} \frac{t^n}{(e^t - 1)(1 - e^{-t})} dt, \quad (1)$$

in which Θ_R is a characteristic temperature usually close to the Debye temperature Θ_D and n is an integer depending on the scattering mechanism. As shown in Fig. 2(b), neither n fixed at 5 for electron-phonon scattering nor an independent variable $n = 2.28$ could follow the temperature dependence in the whole measured range. Therefore, a simple one-channel electron-phonon scattering mechanism could not explain the $\rho(T)$ behavior of ZrTe. By applying magnetic field, $\rho_{xx}(T)$ is enhanced in the whole temperature range. However, different from other known TSMs [6,9,13,24], ZrTe does not have the low-temperature upturn at least when magnetic field is up to 9 T or orders of magnitude increase in magnetoresistivity (MR) at low temperature. For $H \| z$ and $I \| x$ at 9 T, MR = $[\rho(H)/\rho(0) - 1]$ reaches a comparatively small value of 340% at 2 K, while it is ~10% at 300 K. It has been shown that for a TSM compound the magnitudes of MR in different samples are positively correlated to the corresponding RRR values, even obeying a scaling relationship [30,31]. However,

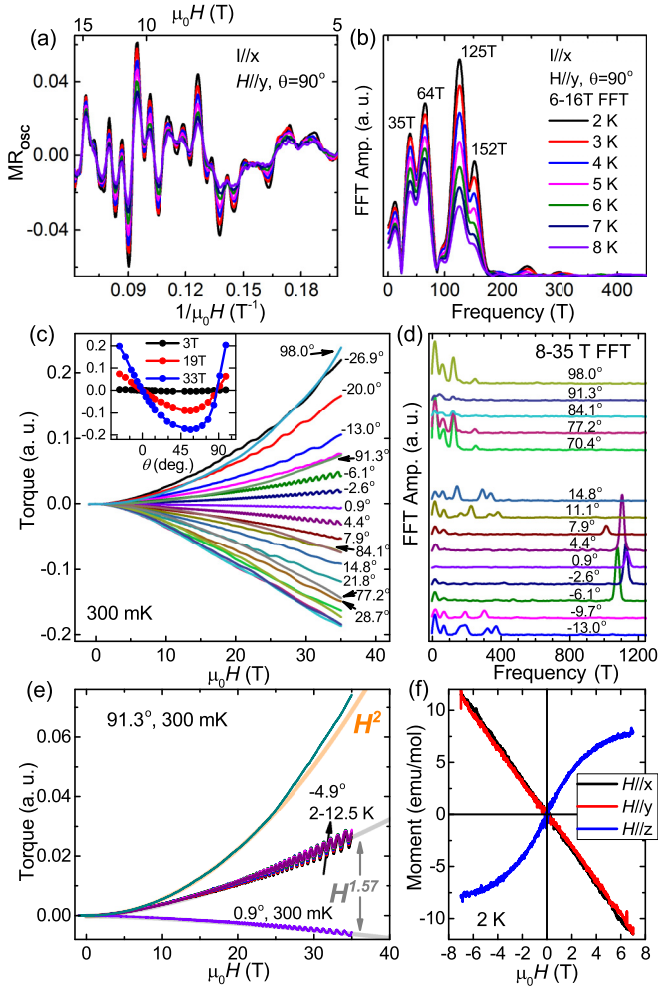

FIG. 3. (a) Oscillating part of MR for $H\|y$ ($\theta = 90°$) at various temperatures and (b) the corresponding FFT spectra. (c) The angle-dependent magnetic torque with sample rotating in the yz plane at 300 mK. The inset shows the angular dependence of the overall torque at selected fields. (d) The stacked FFT spectra of τ_{OSC} around both $H\|z$ (0°) and $H\|y$ (90°). (e) The field dependence of the overall torque signal close to 0° and 90° with different powers of H. (f) The field dependence of dc magnetization with field applied along all three crystalline directions.

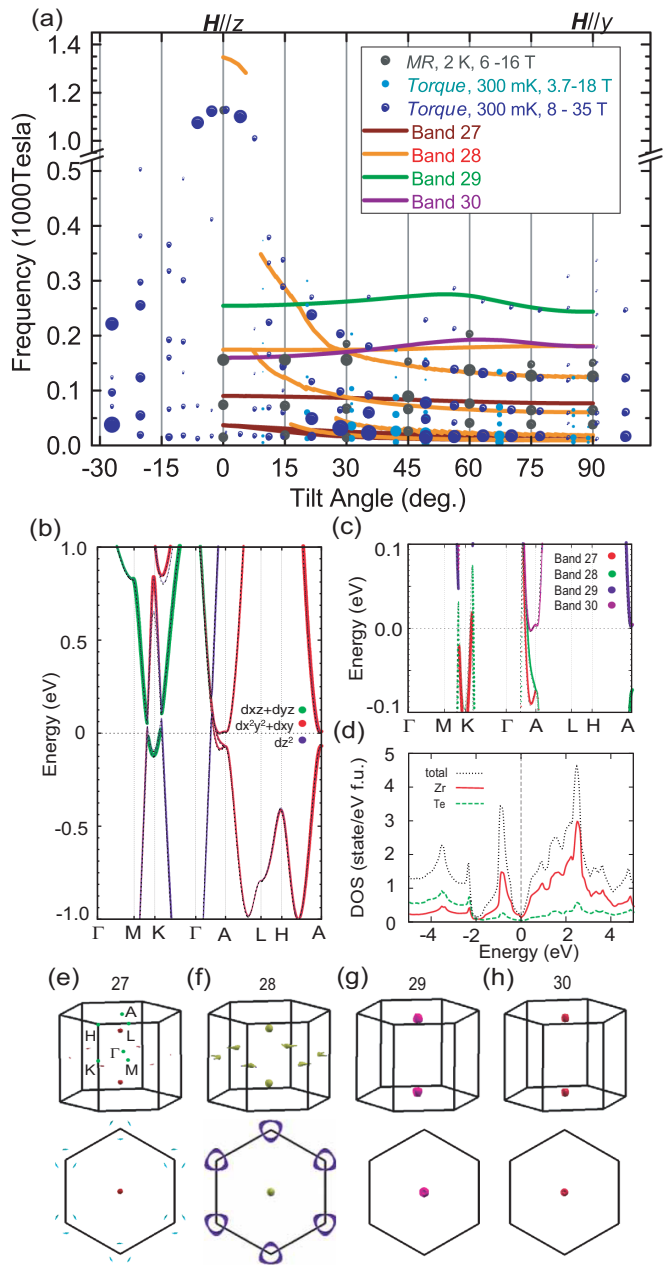

FIG. 4. (a) The angular dependence of quantum oscillation frequencies with magnetic field rotating in the yz plane. Note the break in the vertical scale. The symbol size represents the relative amplitude at a given angle. Frequency dispersions from calculated FSs are superimposed. (b) The calculated band structure of ZrTe by GGA+SOC and (c) the zoom-in part around E_F. (d) The total and partial DOSs per 1 f.u. (e)–(h) Calculated FSs of different bands, each viewed in two perspectives.

since there are different mechanisms that can cause large MR in TSMs, including compensated electrons and holes with high mobility [32] and enhanced backscattering with magnetic field [9], detailed information about the carriers at the FS is needed before we directly link a small MR to a low RRR.

The MRs at 2 K with rotating H in both the yz plane and the xz plane are shown in Figs. 2(c) and 2(d), respectively. As θ varies from 0° to 90°, the absolute value of MR increases first and then decreases, leading to a maximum near $\theta = 30°$ and a minimum at $\theta = 90°$, while in the xz plane MR decreases faster towards 90° and has a maximum anisotropy of ~5. Here the nonmonotonic angular dependence and low anisotropy of MR suggests that ZrTe possesses a complex 3D FS. We note that no negative MR is observed when the magnetic field is parallel to the current, which is similar to the result of WC in the same measurement configuration [24]. However, $\rho_{zz}(H)$ should be examined in a future experiment.

The SdH quantum oscillations are already apparent in Fig. 2. Figure 3(a) shows the isotherms of oscillating magnetoresistivity at $H\|y$ extended to 16 T after a smooth polynomial background substraction. The oscillation periods in $1/H$ are analyzed by fast Fourier transform (FFT). Several frequencies with clear temperature dependence are identified

in Fig. 3(b). The extremal cross-sectional area of a FS is obtained by the Onsager relation [33] $F = (\hbar/2\pi e)A_F$, where A_F is the area in k space, F is the oscillation frequency, $\hbar$ is the reduced Planck constant, and e is the electron charge. The highest frequency here, 151 T, corresponds to an area of 1.44 nm^{-2}, occupying only 0.53% of the projected area of the first Brillouin zone in the k_z-k_x plane. The effective mass m^* is extracted by fitting the temperature dependence of the FFT amplitude of a given frequency by the thermodamping factor $R_T = X/\sinh(X)$ in the Lifshitz-Kosevich (LK) formula [33], where $X = 2\pi^2 k_B T m^*/\hbar eB$, k_B is the Boltzmann constant, T is temperature, and B is the magnetic field strength. Effective masses ranging from $m^* = 0.15m_e$ to $0.26m_e$ are obtained.

Angle- and temperature-dependent measurements of magnetic torque ($\vec{\tau} \equiv \vec{M} \times \vec{B}$) up to 35 T are carried out for detection of dHvA oscillations and are also analyzed within the LK formula. As shown in Fig. 3(c), on the angular dependence data covering over 120°, oscillations are seen on raw curves, in which the torque changes sign at both 0° and 90°. Apparently, a fast-oscillating frequency appears *only* around $H\|z$ (0°). FFT spectra of τ_{OSC} in Fig. 3(d) illustrate that a dominating frequency of ∼1120 T exists within an angle window of about ±8°; in contrast, outside this window all the fundamental frequencies are lower than 400 T. We note that the same frequency is also observed in SdH for $H\|z$, while in torque data it also shows a dispersion, decreasing when away from $H\|z$. Different from the observation in ZrSiS [34], in which those fast QOs happen only at high field due to magnetic breakdown, for ZrTe the fast frequency is readily visible at low field and is more likely from a FS hosting a semiopen cyclotron orbit. The corresponding effective mass is $0.28m_e$ from the temperature dependence of the torque at −4.9° [Fig. 3(e)], indicating that the associated band also has a steep dispersion close to the Fermi level.

In Fig. 4(a), the variation of oscillation frequencies against field direction in the yz plane is mapped, and discrete points from both SdH and dHvA measurements on different pieces of crystals are shown, which are complementary and consistent. In addition to the aforementioned abrupt change in the highest frequency close to $H\|z$, there are multiple groups of points where a frequency change from 0° to 90° can be traced and can tentatively be assigned as fundamental frequencies. Since the frequency dispersion is directly linked to the shape and size of a FS, a comparison with band structure calculations is made in the following.

Our calculated band structure of ZrTe is in general agreement with reported results [17,18,20,35]. There are band inversions along M-K-Γ and Γ-A in the BZ. With spin-orbit coupling (SOC), band degeneracy is lifted, and the band crossing points along M-K-Γ are gapped, while TPs persist along Γ-A, slightly above the Fermi level E_F. As shown in Figs. 4(b)–4(d), there are four bands crossing E_F on high-symmetry lines, labeled from 27 to 30. Bands 27 and 28 form hole-type FSs, and bands 29 and 30 form electron-type FSs. The density of states (DOS) at E_F is mostly contributed by Zr d electrons and is close to a local minimum. Figures 4(e)–4(h) depict FSs constructed by the four bands separately. FSs of band 27 are nested inside those of band 28 since the two bands have the same origin before spin splitting. For the FSs centered on the $k_z = 0$ plane, the valence band maximum of band 27 along M-K is below E_F and results in a spindlelike FS close to K within the first BZ, whereas for band 28, band maximums along both M-K and Γ-K are both above E_F, leading to a thin, toroid FS in view of the extended BZ. We note that this is a particular closed FS that has a semiopen cyclotron orbit: the large orbit cycling the whole ring disappears once the plane normal to the external magnetic field can intersect only a section of the ring. Using the program SKEAF [36], the variation of extremal cross-section areas and effective masses of calculated Fermi surfaces versus the angle are extracted, and corresponding frequencies are superimposed in Fig. 4(a) on experimental data. One branch of frequencies from band 28 shows the abrupt increase within a ±5.5° window at $H\|z$ to a maximum about 1300 T; hence, the origin of the experimental observation is reasonably explained. At the same time, the calculated frequency dispersions are in quantitative agreement with a major portion of experiment data, as well as the effective masses at $H\|z$ and $H\|y$ listed in Table I. So the current band calculation has captured the main character of the bulk electronic structure of ZrTe; a hint for the hole-dominant transport at low temperature can be found from the calculated heavier effective masses of electron bands. Further experiment is needed to probe those missing frequencies. On the other hand, for TSMs in which the band extremal or crossing points are very close to E_F, as in the Weyl semimetal TaP [37], the FS topology is sensitive to calculation details. In the current case, while SOC is essential in determining the band structure, the energy separation at the A point and then the size of electron FSs are largely affected by the strength of SOC.

TABLE I. Comparison of experimentally extracted quantum oscillation frequencies and effective masses to calculated ones. Torque data are taken at slightly off-axis angles to gain signal. The effective masses for $H\|z$ and $H\|y$ are from torque ($\theta = -4.9°$, $F = 1112$ T) and SdH data, respectively. A dash (–) denotes the lack of a corresponding value.

	Experiment			Calculation		
	F_{SdH} (T)	F_{Torque} (T)	m^* (in units of m_e)	F (T)	m^* (in units of m_e)	Band label
$H\|z$	–	–	–	37	0.2	27
	75 ± 3	–	–	–	–	–
	–	–	–	90.2	0.21	27
	157 ± 2	–	–	159.7	1.54	30
	–	–	–	174.4	0.29	28
	–	–	–	254.3	1.82	29
	1130 ± 3	1130 ± 1	0.28 ± 0.04	1347.3	0.43	28
$H\|y$	–	–	–	9.3	0.09	27,28
	–	–	–	18.5	0.13	27,28
	35 ± 1	42 ± 2	0.15 ± 0.01	–	–	–
	64 ± 1.5	61 ± 2	0.14 ± 0.01	60.6	0.15	28
	–	–	–	76.7	0.19	27
	125 ± 1	121 ± 3	0.23 ± 0.01	124.3	0.28	28
	152 ± 2	155 ± 3	0.25 ± 0.02	–	–	–
	–	183 ± 4	–	180.3	3.6	30
	–	–	–	181.3	0.35	28
	–	240 ± 4	–	243.5	4.2	29

Last, we discuss the magnetization properties of ZrTe. The $T = 2$ K field-dependent magnetization curves with field along all three principle axes are presented in Fig. 3(f); the background from the sample holder has been carefully removed. The isothermal curves of $H\|x$ and $H\|y$ are equivalent, diamagnetic, and generally linear in H up to 7 T, whereas for $H\|z$ it is paramagnetic and deviating from linear at low field. This enhanced diamagnetism has been observed in other TSMs like TaAs [38] and ZrSiS [39], which can, in general, be attributed to the existence of Dirac-type electrons as in the element bismuth [40]. The difference in the field dependence of magnetization is also represented in the torque data in Fig. 3(e). For H close to y, the overall torque response can be simulated by a simple H^2 curve with a slight deviation at high field, indicating a linear dependence of magnetization on H, while for H close to z, it is reduced to $\tau \sim H^{1.57}$, where the magnetization is proportional to the square root of the field strength. In addition, the angular dependence of torque at fixed fields confirms that at a given field torque changes faster close to 90° than close to 0°. Whether the anisotropy of magnetization and its field dependence could be connected to the existence of TPs is of high interest. It has been suggested for field applied along the z axis that preserving the C_3 symmetry, the Landau level spectrum of a TP is not gapped, different from that for other directions [17], for which the interband part contributing to the magnetic susceptibility χ is diamagnetic. However, since there are multiple FSs and, moreover, the interband contribution is not necessarily the main part of the total χ [41], calculations of the free energy and magnetization based on the real band structure are needed before any claim can be made. As an extra note, no abrupt change in field-dependent torque curves or their slope has been observed for ZrTe up to 35 T, while in Weyl semimetals [42,43] such a feature exists at the quantum limit and has been claimed to be a signature of the Weyl node.

In conclusion, we have experimentally determined the bulk electronic structure of WC-type ZrTe by a quantum oscillation study; ZrTe has been proposed as a new type of topological semimetal hosting a triply degenerate node. Although it is also a low-carrier-density semimetal, the low-temperature electric transport shows hole dominance, different from other TSMs with electron-hole compensation. In addition, the paramagnetic $H^{0.5}$ dependence of magnetization with H along the C_3 symmetry axis at high field is unique.

ACKNOWLEDGMENTS

We thank H. M. Weng for helpful discussions. G.L. thanks A. Suslov for help during the high-field experiment. This work was supported by the National Basic Research Program of China 973 Program (Grant No. 2015CB921303), the National Key Research Program of China (Grants No. 2016YFA0300604 and No. 2016YFA0300602), the Strategic Priority Research Program (B) of the Chinese Academy of Sciences (Grants No. XDB07020100 and No. XDB33010100), and the Natural Science Foundation of China (Grants No. 11404175, No. 11874417, and No. 11974397). The National High Magnetic Field Laboratory is supported by the National Science Foundation through NSF/DMR-1644779 and the state of Florida.

APPENDIX

Figures 5–8 provide additional data, showing a test of the two-band-model fitting of the temperature dependence of Hall conductivity, the temperature dependence of magnetization, the method used to estimate the error bars of QO data, and a comparison of calculated versus experimentally determined band structures by varying input parameters, respectively.

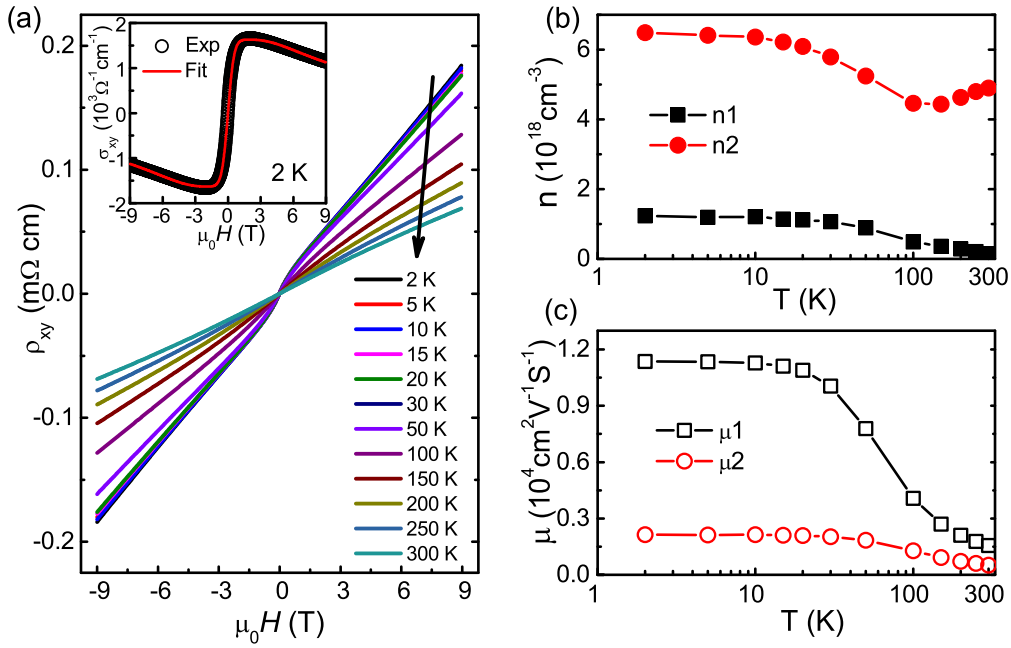

FIG. 5. Hall resistivity and test of the two-band-model fitting. Two hole-type charge carriers are used. (a) The isothermal Hall resistivity up to 300 K, with the inset showing the fitting of Hall conductivity at 2 K. (b) and (c) The extracted carrier concentrations and mobilities, respectively.

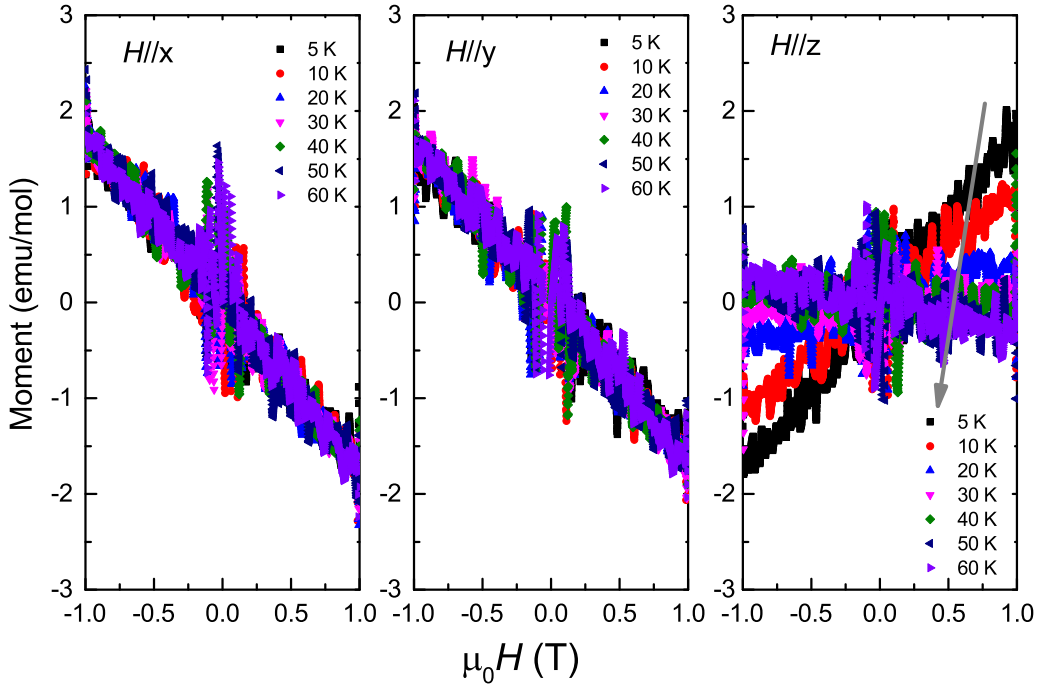

FIG. 6. Isothermal magnetization with field along three different axes up to 60 K. The background originating from the sample holder has been subtracted. Spikes around zero field are due to noise.

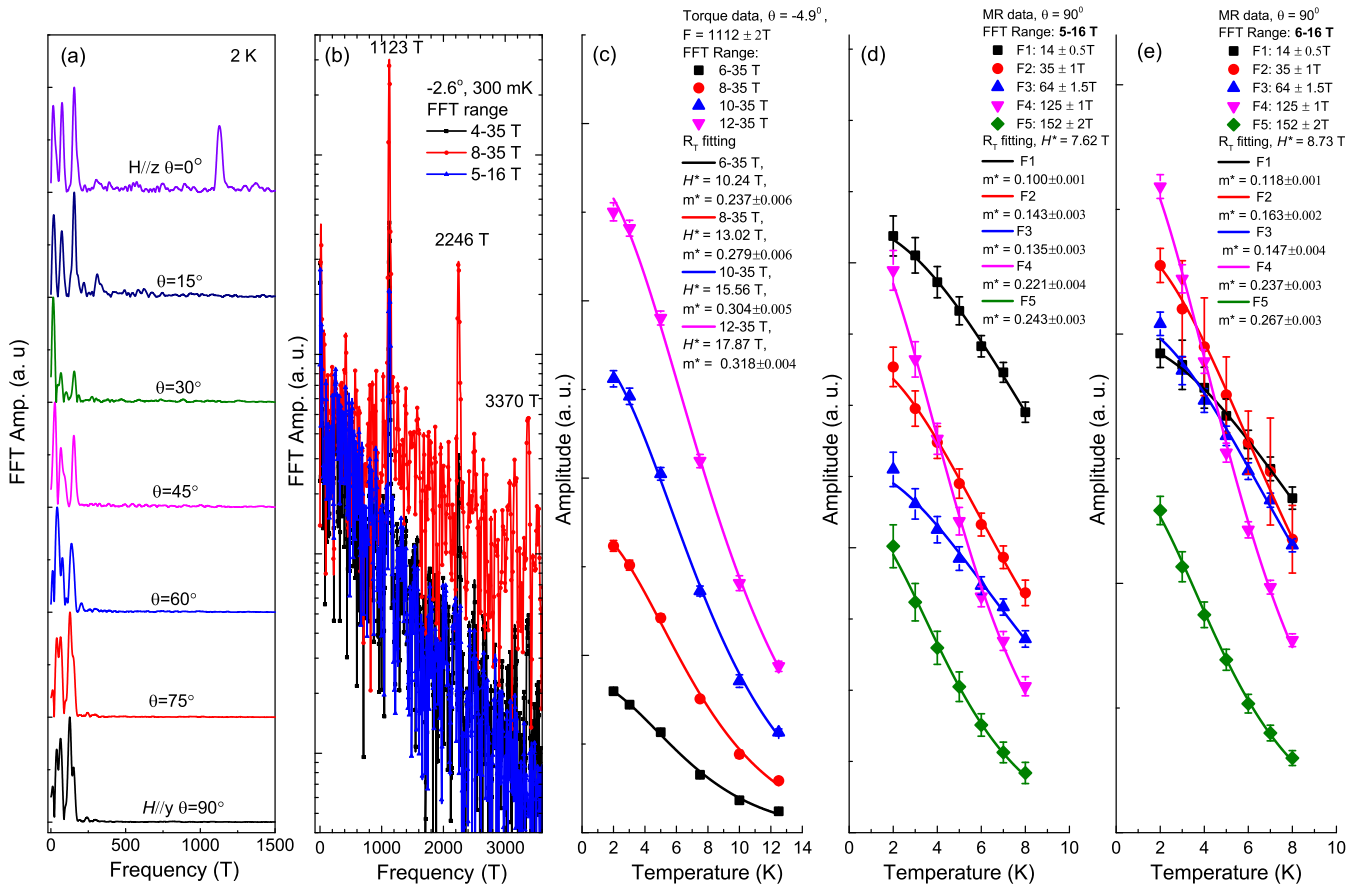

FIG. 7. Analysis of quantum oscillation data. (a) The stacked FFT spectra of angle-dependent SdH data. (b) The FFT spectra of torque data at an angle close to $H \parallel z$ with different FFT field ranges. Note the semilog scale. Harmonics of the prominent peak are observed. (c)–(e) The fitting of thermal damping factor to the temperature-dependent FFT amplitude with varying FFT field range as a method of estimating the error bars in determining effective mass.

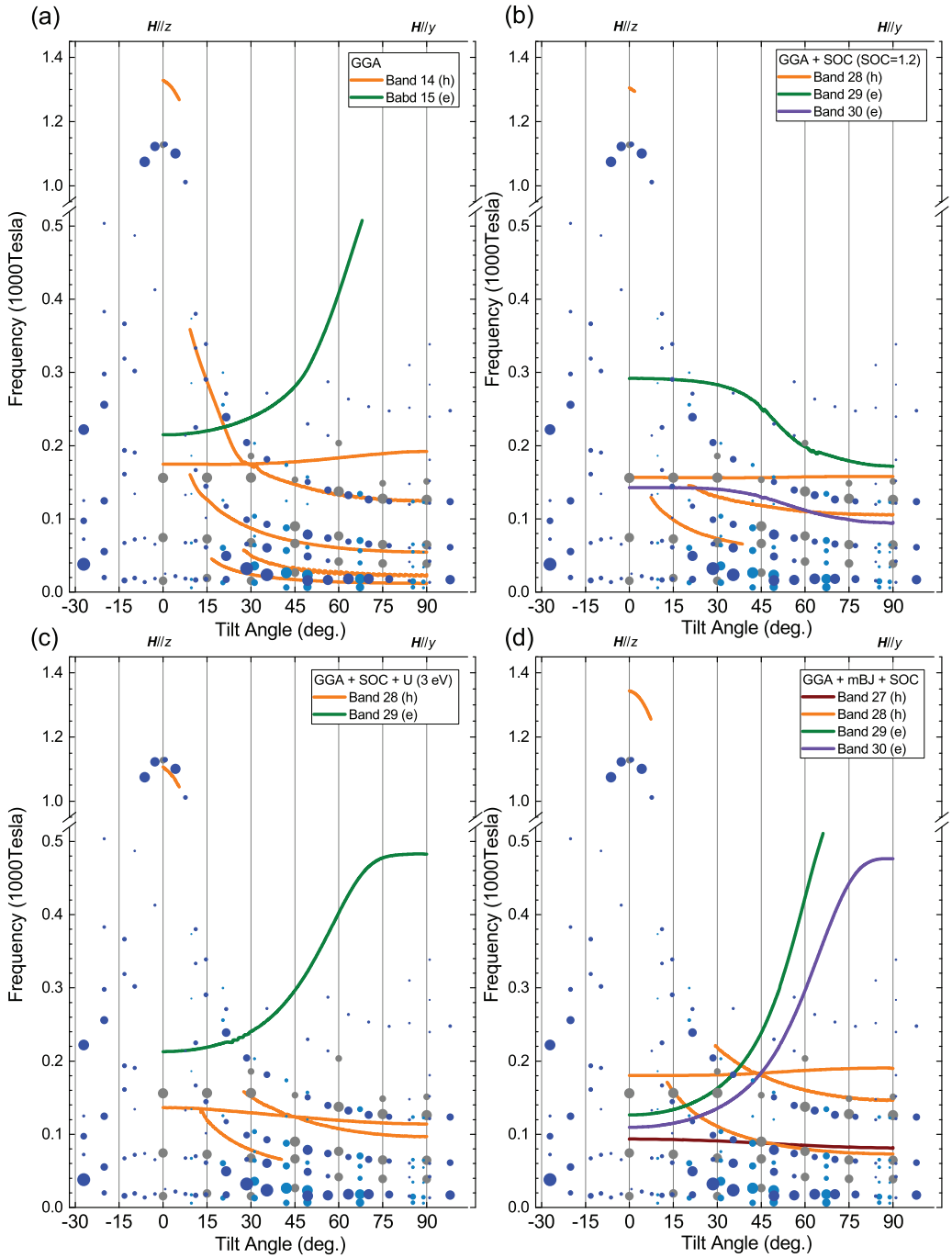

FIG. 8. Comparison of the experimentally extracted angle-dependent quantum oscillation frequencies with dispersions obtained by different calculation methods. There were no other adjusted parameters. (a) By GGA alone the electron Fermi surface (FS) is too large. (b) By increasing SOC too much the size of both electron and hole FSs is reduced. (c) By introducing on-site Coulomb interaction energy, the size of the hole FS is reduced, but the electron FS is still too large. (d) By GGA with modified Becke-Johnson (mBJ) correction and SOC, the electron FS is too large.

[1] H. Weng, X. Dai, and Z. Fang, J. Phys.: Condens. Matter **28**, 303001 (2016).

[2] A. Bansil, H. Lin, and T. Das, Rev. Mod. Phys. **88**, 021004 (2016).

[3] C. K. Chiu, J. C. Y. Teo, A. P. Schnyder, and S. Ryu, Rev. Mod. Phys. **88**, 035005 (2016).

[4] Z. Wang, Y. Sun, X.-Q. Chen, C. Franchini, G. Xu, H. Weng, X. Dai, and Z. Fang, Phys. Rev. B **85**, 195320 (2012).

[5] Z. K. Liu, B. Zhou, Y. Zhang, Z. J. Wang, H. M. Weng, D. Prabhakaran, S.-K. Mo, Z. X. Shen, Z. Fang, X. Dai, Z. Hussain, and Y. L. Chen, Science **343**, 864 (2014).

[6] J. Xiong, S. K. Kushwaha, T. Liang, J. W. Krizan, M. Hirschberger, W. D. Wang, R. J. Cava, and N. P. Ong, Science **350**, 413 (2015).

[7] Z. Wang, H. Weng, Q. Wu, X. Dai, and Z. Fang, Phys. Rev. B **88**, 125427 (2013).

[8] Z. K. Liu, J. Jiang, B. Zhou, Z. J. Wang, Y. Zhang, H. M. Weng, D. Prabhakaran, S.-K. Mo, H. Peng, P. Dudin, T. Kim, M. Hoesch, Z. Fang, X. Dai, Z. X. Shen, D. L. Feng, Z. Hussain, and Y. L. Chen, Nat. Mater. **13**, 677 (2014).

[9] T. Liang, Q. Gibson, M. N. Ali, M. Liu, R. J. Cava, and N. P. Ong, Nat. Mater. **14**, 280 (2015).

[10] S.-Y. Xu, I. Belopolski, N. Alidoust, M. Neupane, G. Bian, C. Zhang, R. Sankar, G. Chang, Z. Yuan, C.-C. Lee, S.-M. Huang, H. Zheng, J. Ma, D. S. Sanchez, B. Wang, A. Bansil, F. Chou, P. P. Shibayev, H. Lin, S. Jia, and M. Z. Hasan, Science **349**, 613 (2015).

[11] H. Weng, C. Fang, Z. Fang, B. A. Bernevig, and X. Dai, Phys. Rev. X **5**, 011029 (2015).

[12] B. Q. Lv, H. M. Weng, B. B. Fu, X. P. Wang, H. Miao, J. Ma, P. Richard, X. C. Huang, L. X. Zhao, G. F. Chen, Z. Fang, X. Dai, T. Qian, and H. Ding, Phys. Rev. X **5**, 031013 (2015).

[13] X. Huang, L. Zhao, Y. Long, P. Wang, D. Chen, Z. Yang, H. Liang, M. Xue, H. Weng, Z. Fang, X. Dai, and G. Chen, Phys. Rev. X **5**, 031023 (2015).

[14] A. A. Burkov, M. D. Hook, and L. Balents, Phys. Rev. B **84**, 235126 (2011).

[15] H. Weng, Y. Liang, Q. Xu, R. Yu, Z. Fang, X. Dai, and Y. Kawazoe, Phys. Rev. B **92**, 045108 (2015).

[16] B. Bradlyn, J. Cano, Z. Wang, M. G. Vergniory, C. Felser, R. J. Cava, and B. A. Bernevig, Science **353**, aaf5037 (2016).

[17] Z. Zhu, G. W. Winkler, Q. S. Wu, J. Li, and A. A. Soluyanov, Phys. Rev. X **6**, 031003 (2016).

[18] G. Chang, S.-Y. Xu, S.-M. Huang, D. S. Sanchez, C.-H. Hsu, G. Bian, Z.-M. Yu, I. Belopolski, N. Alidoust, H. Zheng, T.-R. Chang, H.-T. Jeng, S. A. Yang, T. Neupert, H. Lin, and M. Z. Hasan, Sci. Rep. **7**, 1688 (2017).

[19] H. Weng, C. Fang, Z. Fang, and X. Dai, Phys. Rev. B **93**, 241202(R) (2016).

[20] H. Weng, C. Fang, Z. Fang, and X. Dai, Phys. Rev. B **94**, 165201 (2016).

[21] B. Q. Lv, Z.-L. Feng, Q.-N. Xu, X. Gao, J.-Z. Ma, L.-Y. Kong, P. Richard, Y.-B. Huang, V. N. Strocov, C. Fang, H.-M. Weng, Y.-G. Shi, T. Qian, and H. Ding, Nature (London) **546**, 627 (2017).

[22] N. Kumar, Y. Sun, M. Nicklas, S. J. Watzman, O. Young, I. Leermakers, J. Hornung, J. Klotz, J. Gooth, K. Manna, V. Süß, S. N. Guin, T. Förster, M. Schmidt, L. Muechler, B. Yan, P. Werner, W. Schnelle, U. Zeitler, J. Wosnitza, S. S. P. Parkin, C. Felser, and C. Shekhar, Nat. Commun. **10**, 2475 (2019).

[23] J.-Z. Ma, J.-B. He, Y.-F. Xu, B. Q. Lv, D. Chen, W.-L. Zhu, S. Zhang, L.-Y. Kong, X. Gao, L.-Y. Rong, Y.-B. Huang, P. Richard, C.-Y. Xi, E. S. Choi, Y. Shao, Y.-L. Wang, H.-J. Gao, X. Dai, C. Fang, H.-M. Weng, G.-F. Chen, T. Qian, and H. Ding, Nat. Phys. **14**, 349 (2018).

[24] J. B. He, D. Chen, W. L. Zhu, S. Zhang, L. X. Zhao, Z. A. Ren, and G. F. Chen, Phys. Rev. B **95**, 195165 (2017).

[25] P. Blaha, K. Schwarz, G. K. H. Madsen, D. Kvasnicka, and J. Luitz, *WIEN2K, an Augmented Plane Wave Plus Local Orbitals Program for Calculating Crystal Properties* (Karlheinz Schwarz, Technische Universität Wien, Vienna, 2001).

[26] J. P. Perdew, K. Burke, and M. Ernzerhof, Phys. Rev. Lett. **77**, 3865 (1996).

[27] A. A. Coelho, OPAS ACADEMIC: General profile and structure analysis software for powder diffraction data, Bruker AXS, Karlsruhe, Germany, 2007.

[28] G. Örlygsson and B. Harbrecht, Z. Naturforsch. B **54**, 1125 (1999).

[29] D. Cvijović, Theor. Math. Phys. **166**, 37 (2011).

[30] M. N. Ali, L. Schoop, J. Xiong, S. Flynn, Q. Gibson, M. Hirschberger, N. P. Ong, and R. J. Cava, Europhys. Lett. **110**, 67002 (2015).

[31] C.-L. Zhang, Z. Yuan, Q.-D. Jiang, B. Tong, C. Zhang, X. C. Xie, and S. Jia, Phys. Rev. B **95**, 085202 (2017).

[32] M. N. Ali, J. Xiong, S. Flynn, J. Tao, Q. D. Gibson, L. M. Schoop, T. Liang, N. Haldolaarachchige, M. Hirschberger, N. P. Ong, and R. J. Cava, Nature (London) **514**, 205 (2014).

[33] D. Shoenberg, *Magnetic Oscillations in Metals* (Cambridge University Press, Cambridge, 1984).

[34] S. Pezzini, M. R. van Delft, L. M. Schoop, B. V. Lotsch, A. Carrington, M. I. Katsnelson, N. E. Hussey, and S. Wiedmann, Nat. Phys. **14**, 178 (2017).

[35] S.-D. Guo, Y.-H. Wang, and W.-L. Lu, New J. Phys. **19**, 113044 (2017).

[36] P. Rourke and S. Julian, Comput. Phys. Commun. **183**, 324 (2012).

[37] F. Arnold, C. Shekhar, S.-C. Wu, Y. Sun, R. D. dos Reis, N. Kumar, M. Naumann, M. O. Ajeesh, M. Schmidt, A. G. Grushin, J. H. Bardarson, M. Baenitz, D. Sokolov, H. Borrmann, M. Nicklas, C. Felser, E. Hassinger, and B. Yan, Nat. Commun. **7**, 11615 (2016), Supplementary Materials.

[38] F. Arnold, M. Naumann, S.-C. Wu, Y. Sun, M. Schmidt, H. Borrmann, C. Felser, B. Yan, and E. Hassinger, Phys. Rev. Lett. **117**, 146401 (2016).

[39] J. Hu, Z. Tang, J. Liu, Y. Zhu, J. Wei, and Z. Mao, Phys. Rev. B **96**, 045127 (2017).

[40] Y. Fuseya, M. Ogata, and H. Fukuyama, J. Phys. Soc. Jpn. **84**, 012001 (2015).

[41] M. Ogata, J. Phys. Soc. Jpn. **86**, 044713 (2017).

[42] P. J. W. Moll, A. C. Potter, N. L. Nair, B. J. Ramshaw, K. A. Modic, S. Riggs, B. Zeng, N. J. Ghimire, E. D. Bauer, R. Kealhofer, F. Ronning, and J. G. Analytis, Nat. Commun. **7**, 12492 (2016).

[43] K. A. Modic, T. Meng, F. Ronning, E. D. Bauer, P. J. W. Moll, and B. J. Ramshaw, Sci. Rep. **9**, 2095 (2019).